

**REPORT DOCUMENTATION PAGE**Form Approved  
OMB NO. 0704-0188

Public Reporting burden for this collection of information is estimated to average 1 hour per response, including the time for reviewing instructions, searching existing data sources, gathering and maintaining the data needed, and completing and reviewing the collection of information. Send comment regarding this burden estimates or any other aspect of this collection of information, including suggestions for reducing this burden, to Washington Headquarters Services, Directorate for Information Operations and Reports, 1215 Jefferson Davis Highway, Suite 1204, Arlington, VA 22202-4302, and to the Office of Management and Budget, Paperwork Reduction Project (0704-0188), Washington, DC 20503.

1. AGENCY USE ONLY (Leave Blank)		2. REPORT DATE 15 DEC 2003	3. REPORT TYPE AND DATES COVERED Final 20 Mar 2000 – 19 May 2003
4. TITLE AND SUBTITLE Adaptive Compensation of Atmospheric Turbulence in Ground-to-Ground Laser Communication Systems			5. FUNDING NUMBERS <del>DAAD19-00-0048</del>
6. AUTHOR(S) Frederic M. Davidson			DAAD19-00-1-0048 8. PERFORMING ORGANIZATION REPORT NUMBER
7. PERFORMING ORGANIZATION NAME(S) AND ADDRESS(ES) Johns Hopkins University 3400 N. Charles Street Baltimore, MD 21218			
9. SPONSORING / MONITORING AGENCY NAME(S) AND ADDRESS(ES) U. S. Army Research Office P.O. Box 12211 Research Triangle Park, NC 27709-2211			10. SPONSORING / MONITORING AGENCY REPORT NUMBER  40356-PH 01
11. SUPPLEMENTARY NOTES The views, opinions and/or findings contained in this report are those of the author(s) and should not be construed as an official Department of the Army position, policy or decision, unless so designated by other documentation.			
12 a. DISTRIBUTION / AVAILABILITY STATEMENT  Approved for public release; distribution unlimited.		12 b. DISTRIBUTION CODE	
13. ABSTRACT (Maximum 200 words)  Two silicon based devices were investigated for use as an optical wave-front sensor to provide error signal inputs to an adaptive optic wave-front control system intended to reduce the effects of atmospheric turbulence in ground-to-ground laser communication systems. One device was an active sensor array fabricated in CMOS. The other was a silicon photoconductive optical detector with surface electrodes expected to produce PEMF photocurrents in response to spatial motion of an optical interference pattern that illuminates the region between the surface electrodes. Instead, the predominant photo-response mechanism in silicon was found to be due to the Dember effect, namely photocurrents that flow through the device in short circuit configuration that arise from photoexcited charge carrier concentration gradients formed between the illuminated regions of the semiconductor and the dark, shadowed region directly below the surface metal contact electrodes. The Dember photocurrents depend in a complicated way on fringe position relative to the contact electrodes, fringe spacing, and temporal frequency of sinusoidal phase modulation impressed on one beam. The Dember photo-response characteristics of this type of photodetector were mathematically characterized and experimentally verified for the first time, to the best of our knowledge, by the work performed under this award.			
14. SUBJECT TERMS Silicon photodetectors, Dember photocurrents, optical phase detection			15. NUMBER OF PAGES
			16. PRICE CODE
17. SECURITY CLASSIFICATION OR REPORT UNCLASSIFIED	18. SECURITY CLASSIFICATION ON THIS PAGE UNCLASSIFIED	19. SECURITY CLASSIFICATION OF ABSTRACT UNCLASSIFIED	20. LIMITATION OF ABSTRACT  UL

NSN 7540-01-280-5500

Standard Form 298 (Rev.2-89)  
Prescribed by ANSI Std. Z39-18  
298-102

20040112 077

**Final Progress Report for DAAD 190010048**

**“Adaptive Compensation of Atmospheric Turbulence in Ground-to-Ground Laser  
Communication Systems”**

Frederic M. Davidson  
Department of Electrical and Computer Engineering  
The Johns Hopkins University  
Baltimore, MD 21218

December 2003

**DISTRIBUTION STATEMENT A**  
Approved for Public Release  
Distribution Unlimited

**Problem Statement:**

Atmospheric turbulence causes random phase perturbations to be impressed on phase fronts of laser beams as they propagate from transmitter to receiver. This causes a loss of spatial coherence across the optical wave-front, beam wander, and intensity scintillations at the plane of the receiver. All three of these effects result in an increase in the bit error rate of an optical communication receiver over what would occur if the laser beam propagated through free space. One way to improve receiver performance under these conditions is to use an adaptive optics subsystem to correct the random phase perturbations on the received optical wave-front prior to photo-detection by the receiver. This requires the use of some kind of optical wave front sensor that detects the unwanted phase variations and provides an error signal input to the adaptive optic wave-front compensation system.

Optical phase information can be converted to optical intensity information by forming an interference pattern between a stable optical reference beam with a constant, or non varying, optical phase front and the phase corrupted optical wave-front. An ideal optical wave-front sensor would respond only to motion of the fringes in the interference pattern, and not time varying optical intensity changes not caused by temporal phase variations on the signal beam wave-front. The photo-electromotive force (PEMF) effect in partially compensated photoconductive semiconductors such as gallium arsenide, and indium phosphide, and in bismuth silicon oxide, had previously been shown to produce measurable photocurrents in response to optical phase changes on one of two interfering optical beams and to be insensitive to temporal intensity modulation on either of the two interfering beams.

The basic objective of this award was to investigate the use of the photo-electromotive force effect (PEMF) in silicon as the basis for an optical wave-front sensor that would directly measure optical phase differences. To this end, three sets of silicon photoconductive devices were fabricated and experimentally evaluated for use as an optical wave-front sensor. In addition, a more conventional device in the form of a temporal difference imager fabricated in the form of a CMOS active pixel sensor was investigated. This latter device relied upon a Zernike filter to first shift the optical phase across an optical wave-front by ninety degrees to first convert phase information to intensity information which is then detected by the active pixel array sensor. Subtraction of two consecutive images yields information about the temporal phase changes provided the optical field intensity itself has not changed in each of the two images.

**Summary of Results:**

The design and performance characteristics of the CMOS active pixel image chip are described in the paper entitled "A Pipelined Temporal Difference Imager " contained in Appendix I. The chip was shown to be capable of subtracting two images but with insufficient speed and conversion gain to be useful in detecting atmospheric turbulence induced phase changes across a laser beam wave-front. Improved designs are being pursued under alternative funding sources.

The results of the investigations of the PEMF effect in silicon are described in the paper entitled "Dember and Photo-emf Currents in Silicon Photoconductive Detectors" contained in Appendix II. Silicon photoconductive detectors, with the geometry shown in Figure 1b of the paper in Appendix II, were commercially fabricated on (a) standard n-type silicon wafers, (b) high resistivity, weakly n-type silicon wafers, and (c) as in (b) but proton implanted to shorten the photo-excited charge carrier lifetime. Although sizable photocurrents were observed in the last set of devices, these photocurrents turned out to be due to the Dember effect and not the PEMF effect. Dember photocurrents are due to photo-excited charge carrier diffusion that arises from non spatially uniform illumination of the device and does not require the presence of an internal space charge electric field. PEMF photocurrents do rely on the existence of an internal space charge electric field formed by diffusion of photo-excited charge carriers to regions of lesser illumination where they become trapped. Dember photo-currents exhibit low frequency behavior and vanish as  $\omega\tau \gg 1$ . PEMF photocurrents exhibit high frequency behavior in that the photocurrent increases from zero over the range  $0 \leq \omega\tau_G \leq 1$  and then decreases again to zero as  $\omega\tau \gg 1$ . Here,  $\tau$  is the photo-excited charge carrier lifetime and  $\tau_G \equiv \tau_M$ , the Maxwell, or dielectric relaxation time constant given by  $\epsilon/\sigma_0$  where  $\epsilon$  is the dielectric constant and  $\sigma_0$  is the conductivity. The maximum PEMF photocurrent that can be obtained is proportional to the ratio  $\tau_M/\tau$  if  $\tau$  is much greater than  $\tau_M$ . In high purity silicon, the Maxwell relaxation time is on the order of nanoseconds. Even proton implantation of the high resistivity silicon wafers could not decrease  $\tau$  enough to produce measurable PEMF photocurrents in devices that had surface electrodes.

The use of metallic surface electrodes prevented light from illuminating the region directly beneath them. Consequently, a large Dember photocurrent was generated at the metal – semiconductor edges. In silicon, these Dember photocurrents were measured to be on the order of microamperes, about three orders of magnitude larger than the expected PEMF photocurrents. Because Dember photocurrents can arise from temporal intensity modulation of the optical fields themselves, as well as from spatial motion of optical fringes caused by phase modulation, and are three orders of magnitude larger than the desired PEMF photocurrents, it was concluded that silicon was not a useful material for this kind of optical wave-front sensor. The use of semi-transparent electrodes to reduce the magnitude of the Dember photocurrents was not pursued because of funding limitations of this award.

Dember photocurrents can also exist in GaAs PEMF photodetectors, although they are generally smaller than PEMF photocurrents because of the much smaller (four orders of magnitude) conductivity of semi-insulating GaAs. The work performed under this award did result in the basic characterization of the nature of Dember photocurrents in photoconductive semiconductors operated in a short-circuit configuration, with silicon as the representative photoconductive semiconductor. The Dember response to optical fringe motion caused by sinusoidal phase modulation on the signal beam depends in a complicated way on the position of the fringes relative to the surface contact electrodes, the fringe spacing, and the frequency of the temporal phase modulation. To our knowledge, this is the first such characterization, both theoretically and experimentally, of these types of photocurrents.

**Publications and Technical Reports:**

1. Viktor Gruev and Ralph Etienne-Cummings, "A Pipelined Temporal Difference Imager". *I.E.E. Electronics Letters*, vol.38 (7), pp. 315-317 (2002).
2. Yamac Dikmelik and Frederic Davidson, "Dember and Photo-emf Currents in Silicon Photoconductive Detectors", submitted to *Journal of the Optical Society of America, B*, December, 2003.

**List of Participating Scientific Personnel:**

1. Viktor Gruev (one semester) Ph.D. expected May (2004).
2. Yamac Dikmelik, Ph.D. expected May (2004).
3. Frederic Davidson (PI)

## **Appendix I**

### **A Pipelined Temporal Difference Imager**

## **A Pipelined Temporal Difference Imager**

*Viktor Gruev and Ralph Etienne-Cummings*

Electrical and Computer Engr. Dept., Johns Hopkins University  
105 Barton Hall, Baltimore, MD 21218, USA  
vg@jhu.edu and retienne@jhu.edu  
telephone 410-516-0746

### **ABSTRACT**

A 189 x 182 Active Pixel Sensor (APS) for temporal difference computation is presented. The temporal difference imager (TDI), fabricated in 0.5 $\mu$ m CMOS process, contains in-pixel storage elements for a previous image frame. Difference double sampling circuits are used to suppress the fixed pattern noise in both images and to compute the difference between the corrected images. The pixel area occupies 25 $\mu$ m by 25 $\mu$ m (using 0.7 $\mu$ m scalable rules), with fill factor of 30%. A novel pipelined readout technique is described, which is used to improve the accuracy of the temporal difference computation. With this pipelined read-out architecture, >8 bit precision for the difference image and low spatial droop across the difference image is achieved. The chip consumes 30mW at 50 fps from 5V power supply.

### **1. INTRODUCTION**

The computation of the difference between two temporally displaced images at the focal plane is desirable for many applications. Fast and accurate temporal difference images are required elements of many algorithms in video compression, motion estimation and target tracking. Temporal difference images can be used in segmentation algorithms for extracting moving object from the background scene. Once the moving object has been identified from a scene, efficient video compression algorithms can then be applied [1]. Furthermore, compression algorithms can be applied and optimized independently for the background and the moving objects of the scene. This step allows efficient coding of the image so that a reduce bandwidth is required to transmit real time video. Temporal difference images are also used to correct the phase of wavefronts propagating through turbulent atmospheres. Turbulent atmospheres, produced by heat convection on a hot day for example, in-homogeneously distorts (spatially and temporally) the phase a plane wave propagating though it. Subtracting two consecutive images of the distorted wavefronts, whose phase has been shifted  $(+/-)\pi/2$  by a Zernike filter, however, will produce a difference image where the intensity is proportional to the phase of the wavefront [2]. Once the distorted phases have been measured, adaptive correction techniques, such as stochastic gradient decent, can be applied to correct the distortions [3,4]. For real-time correction, the phase measurement, i.e. the temporal image differencing, must operate at >100fps and with >7 bits accuracy. The chip presented in this paper is intended for the wavefront phase correction application, and will be an essential component in a low error-rate free-space laser communication system.

Temporal difference imagers using photogate and photodiode designs have been reported in the literature. In [5], a photogate design takes advantage of the parasitic capacitance at the readout circuitry to store a previous image, while integrating a new image on the photogate capacitance. Employing special readout timing sequence, temporal difference can be computed for free while acquiring intensity images. These architectures employ fixed integration time of one frame and a fixed time delay between frames. However, the ability to adjusting the exposure time and inter frame time delay are crucial for many applications, especially since the illumination and time constants of motion vary for different applications. In [6], these

shortcomings are addressed, at the expense of the accuracy of the difference. This design contains two storage elements per pixel, allowing for two consecutive images to be sampled and held within each pixel. Although this method provides flexibility for various applications, accuracy of the difference image is strongly effected for long inter frame delays and/or bright illuminations because the effects of leakage currents on the stored images are accentuated in these cases. These leakage currents will drastically reduce the value stored in the storage capacitors, affecting the accuracy of the computed difference. Although various shielding techniques are employed to reduce these leakage currents, they don't completely alleviate the problem. Hence, special read out techniques must be applied to improve the accuracy of the temporal difference.

This paper presents architecture that efficiently and accurately computes the temporal difference between two consecutive images. The integration time and inter frame delay can be easily varied, while the accuracy of the difference of the images is greatly improved by executing a pipeline technique for the difference readout. This pipeline technique minimizes the leakage currents of the storage elements in the pixel, allowing for accurate and reliable temporal difference. Furthermore, it guaranties that the temporal delay between each pixel pair in the stored and current image is constant. Also various shielding techniques are employed to further reduce the leakage currents dependency on illumination. Analysis and measurements results are presented.

## 2. TEMPORAL DIFFERENCE IMAGER ARCHITECTURAL OVERVIEW

### 2.1 System Overview

The TDI consists of four main components: a 189 rows by 182 columns photo pixel array, 2 vertical and 5 horizontal scanning registers, a control timing unit and three difference double sampling units. Each pixel has two outputs: a current frame output and a previous frame output. The two intensity images are presented in parallel to two independent difference double sampling (DDS) circuits, where reset voltage mismatches, kTC noise, charge injection due to switching,  $1/f$  noise and fixed pattern noise (fpn) are suppressed. The difference, between the two corrected intensity images, is computed in a third DDS circuit and presented outside the chip. The control-timing unit synchronizes the timing between all scanning registers and effectuates an efficient pipeline mechanism for computing the difference between the two consecutive images. This unit also controls the integration time of the two frames, the time between two consecutive frames, the sample/hold and computation timing of the difference double sampling circuits. Different readout techniques can be executed by changing bit patterns in the scanning registers and reprogramming the control-timing unit. Hence, a fair comparison between standard readout techniques and our proposed techniques can be made on this imager.

### 2.2 Hardware Implementation

The active pixel sensor (APS) cell, shown in figure 1, is composed of a photodiode, two storage elements C1 and C2, switching transistors, M2-M7, and readout transistors, M8 - M11. A PMOS transistor, M1, is used to control the operation modes of the photodiode. This transistor increases the output voltage swing of the pixel by allowing the reset voltage level of the photodiode to be  $V_{dd}$ . Also, image lag due to incomplete reset, which is evident when an NMOS reset transistor is used, is eliminated by using PMOS reset transistor [7]. The increased output voltage swing comes at the expense of larger pixel area. Using mainly PMOS transistors in the pixel, except for the output source follower transistors, minimized the latter side effect. The NMOS source followers transistors (M8 and M10) ensures the voltage swing is between  $V_{dd}-V_{th}-V(I_{bias})$  of this transistor



and the minimum voltage for the bias transistor for the follower to remain in saturation. In the traditional APS, the maximum output is described by equation (1).

$$V_{out\ max} = V_{dd} - V(I_{photo\ decay}) - V_{th,M8} - V(I_{bias}) \quad (1)$$

Hence, the voltage swing is maximized at the expense of larger pixel size and the design can be safely used at lower supply voltage levels.

The two sample and hold circuits are composed of a sampling transistor M2(M7) and a capacitor C1(C2), implemented with a transistor by connecting the source and drain to  $V_{ss}$ , while the bulk is connected to  $V_{dd}$ . Hence, the effective storage capacitance is the parallel combination of  $C_{gb}$ ,  $C_{gd}$  and  $C_{gs}$ , where g,d,s and b are gate, drain, source and bulk of this transistor respectively, yielding the maximum possible storage capacitance for the given transistor. The extra storage capacitance in the pixel will reduce linearly the photo conversion rate, while the kTC noise is improved only by square root. Hence, the overall SNR will be reduced. The sampling of the photo voltage alternates between the two sample and hold circuits during consecutive frames. Once the stored charge in C1 and C2 are read out to the difference double sampling (DDS) circuits, the pixel is reset and transistors M3 through M6 are turned on to discharge the holding capacitors C1 and C2. Transistors M3 through M6 allow for individual pixels to be reset instead of row wise pixel reset which is common in standard APS. The reset voltage is subtracted from the integrated values in two independent DDS circuits, eliminating the voltage offset variations due to the output source follower. This technique, known as difference double sampling, improves the noise characteristics of the image. The use of two independent DDS circuit for the entire imager further improves the precession accuracy by eliminating row FPN which must be eliminated if row or column parallel DDS is used. After the images have been corrected, the two frames are subtracted in a third DDS circuit and the difference together with the two intensity images are provided outside the chip.

### 2.3 Pipeline Readout Technique

The control-timing unit is a crucial part for synchronizing the different events executed in the imager. This unit controls the pipeline mechanism implemented on the chip, which consists of four stages. The timing diagram of the four stages is presented in figure 2. The horizontal axis presents the timing events in one frame, while the vertical axis represents different pixels across the imager. Hence, four different tasks (stages) can be performed at the same time across different parts of the image plane. In the first stage of the pipeline, the photo voltage is integrated and sampled just before the beginning of stage 2 on capacitor C2. Increasing or decreasing the number of integration columns in stage 1 can vary the integration period. In the second stage of the pipeline, which consists of a single row, the previously stored photo voltage on C1, the newly integrated photo voltage on C2, and the reset values are read out to the DDS circuit. The difference C2-C1 is evaluated after the subtraction of the reset offset from the stored values.

The stored photo voltage on C1 is held for the entire integration period of C2. Due to the leakage currents at the holding node, this value will be less then its original value. The integrated photo voltage sampled on C2 will not be degraded because the difference of the two values is evaluated as the integration period of C2 is completed. Therefore, the minimum difference between these two values will be the magnitude of the decay of C1, which will be the same for all pixels in the imager. This is

very important in order to have good precision in the difference image and an offset in the difference computation can be accounted for across the entire image in the final result.

In the third stage of the pipeline, no operations (NOPs) are executed. The length of this stage can vary between zero and the scanning time of one entire frame. When the integration time of stages one and four are equal to the time to scan half of the columns in the imager, stage three does not exist. When the integration period of stages one and four are one column time, the NOP stage will be close to the scanning time of an entire frame. This stage adds some flexibility in overlapping two integration processes on the entire imager at the same time, while controlling the integration time of each frame independently of each other. The integration times of stages one and four can be the same or different, depending of the application requirement. In most cases, the integration times of these stages are equal.

In the fourth stage, the photo voltage is integrated and sampled on capacitor C1. Increasing or decreasing the number of integration columns in the fourth stage can vary the integration period. Once the integration period is complete, the integrated value is stored and held in C1. The holding time of C1 value only depends on the integration time of stage one and it is the same for all pixels across the imager. Stages one and four of the pipeline cannot overlap, limiting the maximum integration time of both stages to half of the scanning time of one image frame. The pipeline readout mechanism described above, allows for continuous difference evaluation, as each consecutive frame is readout.

This pipeline mechanism improves the precession of the evaluated difference. First order approximation of the difference precision strongly depends on the leakage currents at the holding nodes of C1 and C2. These leakage currents are functions of two factors: holding time and illumination. In order to weaken the dependency on illumination, various layout techniques were applied, such as symmetric layout to ensure equal leakage currents on both holding nodes and various metal shielding techniques. Our pipeline readout mechanism cannot eliminate this problem. The time dependency of the leakage currents, on the other hand, was improved with the pipeline readout mechanism by ensuring that the time delay between the two images are equal for all pixels. Hence, each pixel integrates for equal amount of time and also the holding time is equal for every pixel. Since the holding time of the charge in C1 and C2 are equal and the leakage currents for all pixels can be approximated to be equal then the offset in the temporal difference can be canceled in the final computation. Assuming that the two stored values in capacitor C1 and C2 are the same ( $V_C$ ), the offset in the temporal difference across every pixel is described by equation (2).

$$\text{Max voltage offset for pixels} = V_{C1} - V_{C2} = (V_C - \Delta V_{leakage}) - V_C = \Delta V_{leakage} = \text{NOP} \cdot I_{leakage} / C_{storage} \quad (2)$$

In equation (2),  $V_{C1}$  is the voltage stored on capacitor C1,  $V_{C2}$  is the voltage stored on capacitor C2,  $\Delta V_{leakage}$  is the decay of the value stored in capacitor C1,  $I_{leakage}$  is the reverse diode leakage current and NOP is the holding time of the stored charge in capacitor C1 or C2. Equation (2) states the voltage offset error across the entire imager is independent of the pixel position; hence the error will be an equal offset across the entire imager.

#### 2.4 Snap Shot and Evaluate Mode

The TDI can also operate in a snap shot and evaluate mode. This mode of operation is shown in figure 3. In this mode, first the photo voltage is integrated on capacitor C1. Then a new photo voltage is integrated on capacitor C2. Once the second integration is completed, the difference between the two stored values is evaluated. Since the difference evaluation is computed

in a sequential manner, the holding interval of C1 will increase as the image is scanned out. When the first pixel is evaluated, capacitor C1 has decayed by the integration time of C2. For each additional evaluation of the difference, an additional hold time is introduced. The last pixel will have the maximum hold time described by equation (3).

$$\max \Delta t = t(\text{int of } C2) + M \times N \times t_{clk} \quad (3)$$

In equation (3),  $t(\text{int of } C2)$  is equal to the integration time of C2, while M and N are the size of the imaging array. This additional hold time, which increases for each scanned pixel, introduces a different offset error for each pixel. Ignoring the light intensity dependency of this offset error, the offset should be linearly increasing across the entire imager. This readout technique will require offline calibration and correction, which may not be suitable for application requiring direct and fast computation of temporal difference [7].

### 3. RESULTS

Real life images from the TDI are shown in figure 4(a-b). One of the two intensity images is shown on the left side, while the absolute difference is shown on the right side. The contour of the moving subjects in figure 4(a) is clearly visible in the difference image. Figure 4(c) shows the temporal differences of a grayscale wheel under different rotational speeds. The grayscale wheel contains 36 different grayscale values, with 10 degrees spatially distribution and constant grayscale increments. In the first case (the first image on the left in figure 4(c)), the grayscale wheel is rotated slowly and the temporal difference image records only a small difference between the two consecutive images. Due to the abrupt difference between the first and last grayscale values on the grayscale wheel, the temporal derivative computes high difference in this border region. The temporal difference in the rest of the image is constant and low due to the constant grayscale increments. As the rotational speed of the grayscale wheel is increased, the temporal difference image shows greater difference (overlap) between two consecutive images. In the last case, when the rotational speed is the highest, wide region of high temporal difference values is recorded. The temporal difference in the rest of the image also has higher values compared to the previous cases when the wheel was rotated at slower speeds. This is due to increased overlap between the two consecutive images, which lead to higher temporal difference values.

Figure 5(a) and 5(b) demonstrates the leakage at the holding nodes as a function of light intensity. Figure 5(a) presents several different discharge curves at the holding node C1 for different light intensities. For low light intensities ( $10^{-2} \text{uW/cm}^2$ ) and medium ( $10^2 \text{uW/cm}^2$ ) light intensities the slope of the discharge curves are negligible, allowing for less than 10mV/sec decay (figure 5(b)). This decay rate allows even for slow frame rates of 3fps, a temporal difference precision of 8bits. For very high illumination intensities, the slope of the discharge currents increases to about 100mV/sec. The parasitic reverse diodes at the holding node are in deep reverse bias, which result in high leakage currents. When operating the TDI at 30fps with 100mV/sec decay rate, a temporal difference with 8bit accuracy can be computed (3V output swing of the pixel and a 12bit low noise ADC was used to digitize the image). Equation (4) indicates the bits of precision as a function of decay rate, frame rate and voltage swing of the pixel.

$$\text{error (\%)} = \frac{\text{decay rate}}{\text{fps} \times \text{voltage swing}} \times 100 \quad (4)$$

The leakage currents at the holding nodes limit the precision of the temporal difference. If a snap-shot and evaluate readout technique is used, this precision will be further degraded. The pipeline readout technique helps eliminate this problem. This advantage of the pipeline readout technique is shown in figure 6. The TDI is operated in two different readout modes. The first mode is the snap shot and evaluate mode, which is usually discussed in the literature [5], [6]. In this mode, two consecutive snap shots are obtained and the difference is computed afterwards. In this operation mode, the leakage currents strongly influence the accuracy of the computed difference. As the difference is computed, the first pixel evaluated will have the least holding time and minimum leakage. As the image is evaluated, each additional pixel will have additional time leakage. The last pixel evaluated in the image will have the longest time delay. The leakage currents in this pixel will greatly affect the accuracy of the evaluated difference. The accuracy of this difference across the imager is demonstrated in figure 8-a. The slope is evident in both X and Y direction, as the image is scanned and the difference is evaluated.

The second mode of operation, the TDI takes advantage of the pipeline architecture. Since all pixels will have the same holding time when operating in this mode, the variation due to leakage currents of the difference is minimized. The result of this minimization across the imager can be seen from figure 6-b. The mean difference in this case is 16.5mV with 0.14% variations of the maximum value. The advantage of the pipeline architecture over the snap shot operational mode is evident from the results presented in figure 6.

The total power consumption of 30mW (with three DDS circuits each consuming 9mW of power) at 50fps with fixed pattern noise of 0.6% of the saturation level, makes this imager attractive for many applications. The >8 bit precision for the difference between two consecutive images and the relatively low fpn are the major advantages of this architecture.

#### 4. CONCLUSION

A 189 x 182 pixel CMOS APS imager is described in this paper. The imager provides two intensity images together with temporal difference image. This imager employs an efficient pipelined architecture for computing the difference, ensuring equal integration and storage time of all pixels. The two storage elements per pixel allow for easy computation of the temporal difference. The fix pattern noise of the intensity image is 0.6% and an 8 bit temporal difference can be computed at 50fps. The low power consumption of 30mW at 50fps is a great advantage of this chip. For application in phase correction of wavefronts in turbulent atmospheres, the speed and conversion gain of the imager must be improved.

#### 5. ACKNOWLEDGEMENT

This work is supported by an ARL collaboration grant and NSF award number #ECS-001-0026.

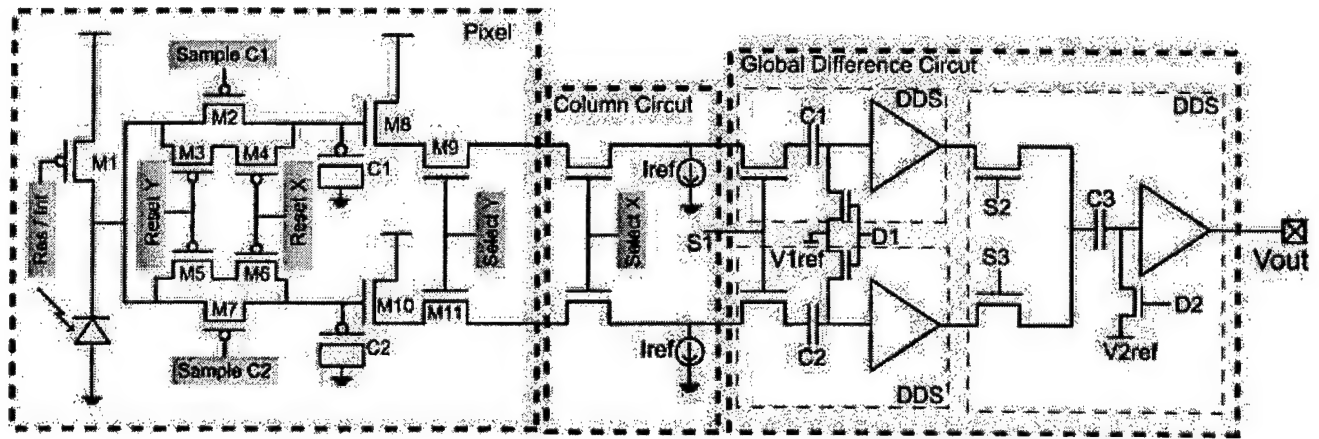


Figure 1: Readout circuit for temporal difference imager

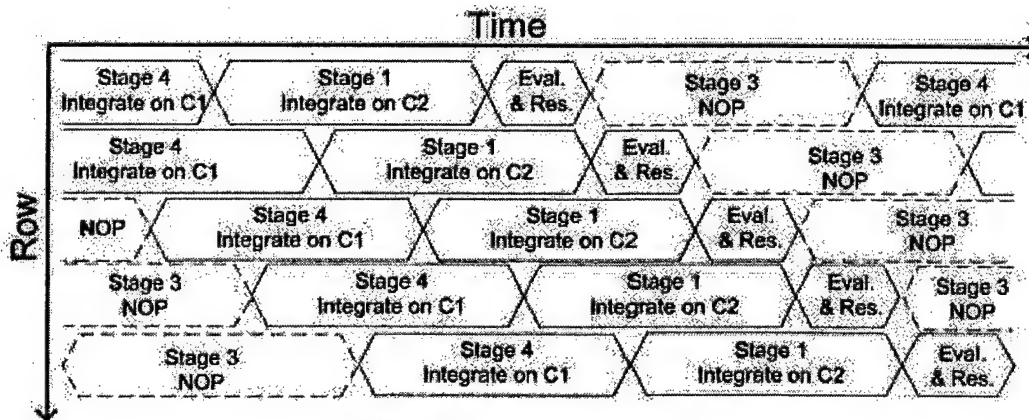


Figure 2: Pipeline Timing

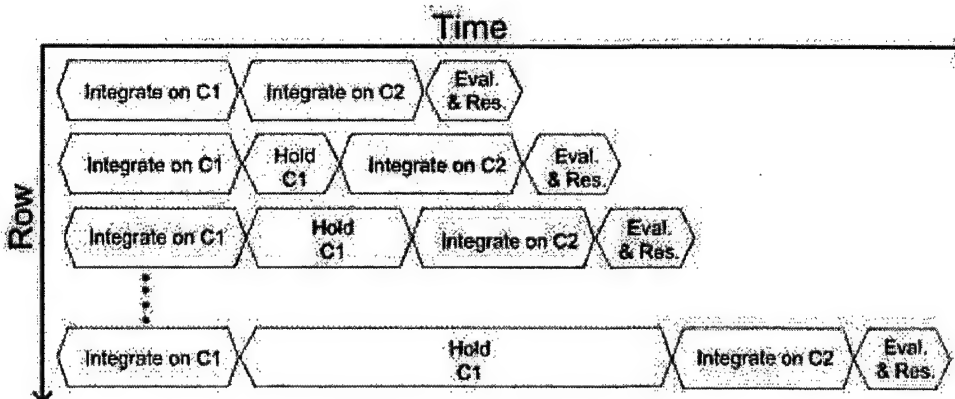


Figure 3: Snap shot and evaluate mode

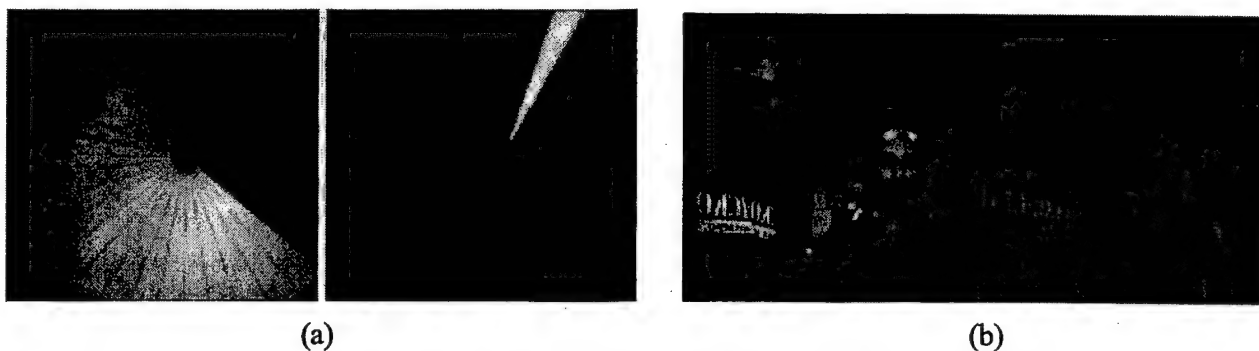


Figure 4 (a) and (b): Sampled intensity and difference images from the TDI

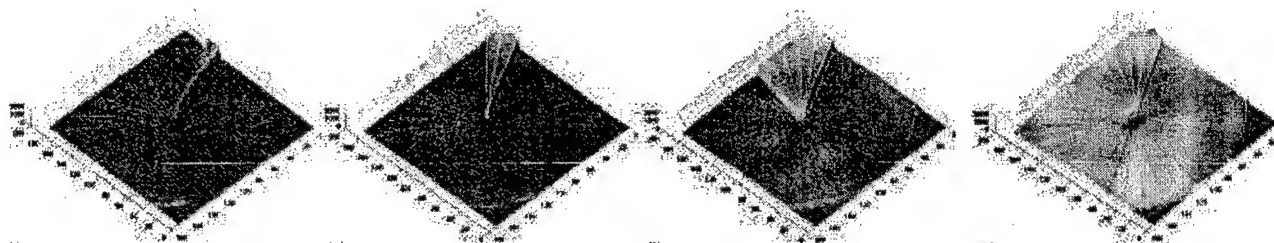
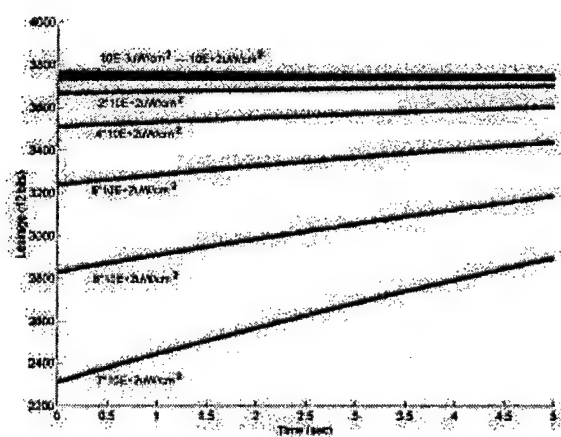
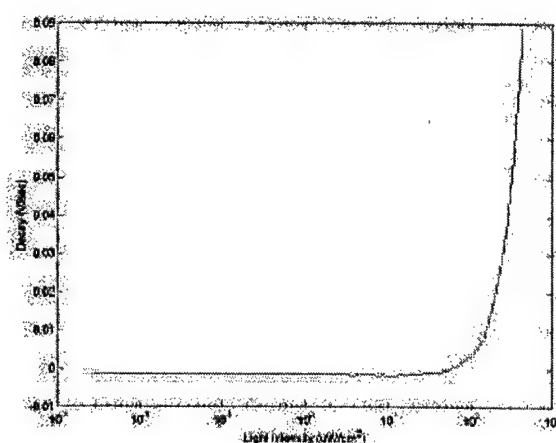


Figure 4 (c): Temporal Difference and its histogram of grayscale wheel under different rotating speed



(a)



(b)

Figure 5 (a): Leakage Currents and (b) decay of stored value

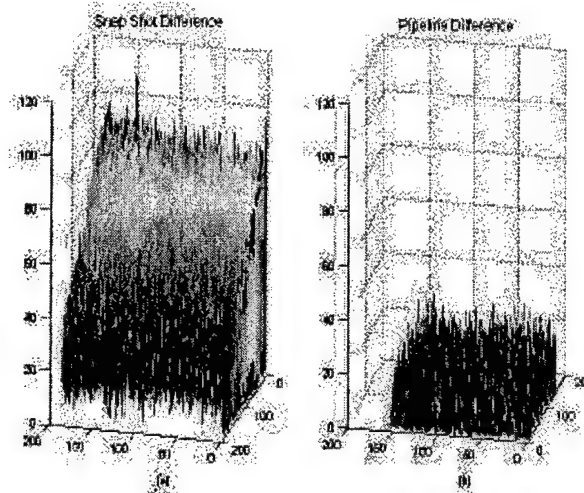


**Figure 6: Comparison between Snap Shot and Pipelined mode of operation at 150mW light intensity**

## 6. REFERENCES

- [1] R. Gonzalez and R. Woods, *Digital Image Processing*. Reading, MA: Addison-Wesley, 1992.
- [2] G.W. Carhart, M.A. Vorontsov, and E.W. Justh, "Opto-electronic Zernike Filter for High-Resolution Wave Front Analysis Using a Phase-Only Liquid Crystal Spatial Light Modulator," In *Proc. of Society of Photo-Optical Instrumentation Engineers*. 2000, pp. 138–147, San Diego, CA, 2000.
- [3] M.H. Cohen, G. Cauwenberghs, M.A. Vorontsov, and G.W. Carhart, "Microelectronic Very Large Scale Integrated Systems for Adaptive Optics and Advanced Imaging," In *Proc. of Society of Photo-Optical Instrumentation Engineers*. 2000, pp. 148–155, San Diego, CA, 2000.
- [4] R.T Edwards, M.H. Cohen, G. Cauwenberghs, M.A. Vorontsov, and G.W. Carhart, "Analog VLSI Parallel Stochastic Optimization for Adaptive Optics," *Learning on Silicon*, pp 359–382. Kluwer Academic, Boston, Dordrecht, London, 1999.
- [5] A. Dickinson, B. Ackland, E.-S. Eid, D. Inglis and E. R. Fossum, "A CMOS 256 X 256 Active Pixel Sensor With Motion Detection," in *Proc. IEEE Int. Solid State Circuits Conference*, 1996, pp. 226–227.
- [6] S. Ma and L. Chen, "A Single-Chip CMOS APS Camera with Direct Frame Difference Output," *IEEE Journal of Solid State Circuits*, vol. 34, pp. 1415–1418, Oct. 1999.
- [7] M.A. Vorontsov, G.W. Carhart, M.H. Cohen, and G. Cauwenberghs, "Adaptive Optics Based On Analog Parallel Stochastic Optimization: Analysis and Experimental Demonstration," *J. Opt. Soc. Am A*, 17(8): pp. 1440–1453, 2000.

## **Appendix II**

### **Dember and Photo-emf currents in Silicon Photoconductive Detectors**



# **Dember and Photo-emf Currents in Silicon Photoconductive Detectors**

**Yamaç Dikmelik and Frederic M. Davidson**

Johns Hopkins University

Department of Electrical and Computer Engineering

Baltimore, MD, 21218

Dember and photo-emf currents are investigated in silicon photoconductive detectors both theoretically and experimentally. Dember photocurrents were found to dominate the response of high-purity silicon samples with top surface electrodes to a moving interference pattern. The use of surface electrodes leads to shadowed regions beneath the electrodes and Dember photocurrents appear under short circuit conditions. A single charge carrier model of the Dember effect is in good qualitative agreement with experimental results. We also show theoretically that the photo-emf effect in Si is weak compared to other semiconductors because of its relatively high intrinsic conductivity.

*OCIS codes:* (040.5150) Photoconductivity; (040.6040) Silicon

## **1. Introduction**

Homogeneous silicon photoconductors exhibit several response mechanisms when exposed to light of photon energy greater than the band gap of 1.1 eV. The most well known is that of a simple photoconductor in which light photo excites electrons and holes which are collected by an

external bias electric field to form an output photocurrent. Another mechanism is the Dember effect<sup>1</sup> in which an open circuit voltage is developed across a bulk sample in response to a nonuniform generation or recombination of charge carriers. If the sample is operated in "short-circuit" mode, in which electrodes on opposite sides of a spatially varying illuminated region are maintained at the same potential (usually ground), then an external photocurrent is generated due to the diffusion of photo excited charge carriers from bright to dark regions in the sample. This photocurrent must have a non zero value in order to maintain the "short-circuit" condition under spatially non-uniform illumination. A third response mechanism is due to the photo-electromotive force effect<sup>2, 3</sup> (PEMF). The bulk sample is again operated in "short-circuit" configuration and is illuminated by a stationary spatially sinusoidal varying optical intensity pattern usually formed by the interference of two mutually coherent optical fields. The diffusion of photo excited charge from bright to dark regions of the interference pattern generates an internal space charge electric field that forms on a time scale,  $\tau_G$ , on the order of the dielectric relaxation time  $\tau_M = \epsilon/\sigma_0$  where  $\epsilon$  is the dielectric constant and  $\sigma_0$  is the conductivity. If the optical fringe pattern moves on a time scale short compared to  $\tau_G$ , the spatially fixed space charge field causes an external current to flow in order to maintain the "short-circuit" condition of zero volts between the contact electrodes. The new spatial distribution of photo excited charge carriers caused by the shift in spatial position of the optical fringes is forced to move by the internal space charge field to form a transient drift current that constitutes the external current flow. The current flow ceases when the internal space charge field has reformed in relation to the new spatial distribution of photo excited charge carriers.

The normal photoconductor current, which requires an external bias field across the semiconductor sample, exhibits a frequency response that extends from DC to some cut-off

frequency dependent on the photo excited charge carrier lifetime,  $\tau$ . The Demer photocurrent, which does not require an external bias field, was also found to exhibit a similar frequency response. The PEMF current however exhibits only a high frequency response in that it increases as  $\omega\tau_G$  for  $0 < \omega < \tau_G^{-1}$ , reaches a plateau, and then decreases to zero as  $\omega\tau$  becomes large. This property makes PEMF detection very useful for measuring rapid (on time scale  $\tau_G$ ) phase changes on one of the two interfering optical beams that form the spatially varying intensity pattern. Photo-emf detectors are usually operated in a short-circuit mode, in contrast to photoconductive detectors operated under a DC bias. For this reason, photo-emf detectors do not respond to overall changes in intensity and suppress intensity fluctuations of the laser<sup>4</sup>. Applications have included velocimetry<sup>4</sup> and nondestructive evaluation<sup>5,6</sup> based on laser-induced ultrasound.

The original PEMF experiments<sup>2</sup> were performed on bulk samples of BSO (a member of the sillenite family of crystals) with electrodes on the sides of the sample as shown in Figure 1 (a). Later, experiments were performed on bulk samples of chrome doped<sup>7</sup> and undoped<sup>8</sup> gallium arsenide and iron doped indium phosphide<sup>8</sup> with light of photon energy below the bandgap energy of the bulk semiconductor. The responsivity in terms of PEMF photocurrent per watt of incident optical power was observed to be very low, on the order of  $10^{-4}$  A/W. In an attempt to improve PEMF responsivity, surface electrodes were used on undoped GaAs samples as shown in Figure 1 (b), illuminated with light of photon energy larger than the bandgap energy. This yielded better responsivity and devices with multiple interdigitated surface electrode configurations were shown to produce PEMF currents that increased linearly with the number of electrode pairs, up to 32 pairs<sup>9</sup>. Overall responsivity however remained below  $10^{-3}$  A/W.

The work reported here describes results obtained with high purity (3000-7000 ohm-cm resistivity), weakly n-type silicon samples with surface electrodes illuminated by 850 nm light where the responsivity of silicon is near its maximum value. The PEMF effect had been observed earlier in bulk samples of silicon<sup>10</sup> with side electrodes as in Figure 1 (a), illuminated with 1064 nm light where the optical absorption constant for silicon is about  $10\text{ cm}^{-1}$ . The PEMF photocurrent observed was quite small, on the order of a few nanoamperes from a 9 mm x 8 mm sample of thickness 0.8 mm, illuminated by about 100 mW of optical power. The use of surface electrodes (or multiple pairs of surface electrodes) and 850 nm light where the optical absorption constant for silicon is on the order of  $10^3\text{ cm}^{-1}$  was expected to improve the PEMF current responsivity.

This was not found to be true for the following reasons. The use of surface electrodes on the illuminated part of the device causes a shadowed region to form directly beneath the electrodes. It is straightforward to form ohmic metallic contacts to silicon. However diffusion currents (Dember currents) form at the boundary between the illuminated semiconductor and the dark region beneath the metal electrode. While these appeared to be small relative to the PEMF currents in GaAs because of its small intrinsic conductivity, they were found to be quite large when compared to the PEMF currents in silicon because of its much larger conductivity even in nearly intrinsic samples. One of our results in this paper is that the photo-emf effect in Si is weak because of its relatively high intrinsic conductivity.

Section 2 of the article reviews the mathematical details of the PEMF response characteristics of high resistivity silicon devices with ohmic surface electrode contacts. Section 3 presents the mathematical details of the short-circuit Dember photocurrent response. Section 4 describes the results of experiments conducted to investigate the response characteristics. Section

5 summarizes the results and gives some conclusions about the usefulness of silicon PEMF devices.

## 2. Photo-emf Current in Si Photoconductive Detectors

We consider a single-carrier model of the photo-emf effect, where the interference pattern is assumed to generate only one type of charge carrier<sup>11</sup>. The recombination process is modeled by assuming a constant recombination lifetime ( $\tau$ ) for this charge carrier<sup>12</sup>. Since the photon energy is larger than the bandgap energy in our experiments, the interference pattern generates electron-hole pairs. However, the single-carrier model has been shown to provide an accurate description of the photo-emf frequency response under most conditions. This model was discussed previously in the literature<sup>11</sup>. Here, we consider the two limiting cases where the carrier lifetime is either much longer or much shorter than the dielectric relaxation time and examine the effects on the amplitude of the photo-emf current. The dielectric relaxation time is much longer than carrier recombination times in typical photo-emf experiments with GaAs detectors. On the other hand, Si detectors have a short dielectric relaxation time because of their high conductivity and correspond to the other extreme.

The interference pattern is formed by two beams intersecting at an angle with each other, as shown in Figure 2. Sinusoidal phase modulation of one of the beams is used to obtain a moving interference pattern that generates the photo-emf current. The intensity of such an interference pattern can be represented by

$$I(x,t) = I_0 [1 + m \cos(Kx + \Delta \cos \omega t)] \quad (1)$$

where  $m$  is the fringe modulation index,  $K = 2\pi/\Lambda_G$  is the wavenumber corresponding to the fringe spacing  $\Lambda_G$ , and  $\Delta$  and  $\omega$  are the amplitude and the frequency of the phase modulation, respectively.

The photo-emf current density is a sinusoidal oscillation at frequency  $\omega$  under periodic boundary conditions<sup>3</sup>. This photo-emf current density can be expressed as

$$J_{\Sigma}(t) = \frac{J^{\omega}}{2} e^{j\omega t} + \frac{J^{\omega*}}{2} e^{-j\omega t} = \text{Re}\{J^{\omega} e^{j\omega t}\} \quad (2)$$

where the complex amplitude of the photo-emf current density is given by<sup>11</sup>

$$J^{\omega} = \frac{m^2 \Delta}{2} \sigma_0 E_D \frac{-j\omega\tau_M}{1 - \omega^2\tau\tau_M + j\omega[\tau + \tau_M(1 + K^2 L_D^2)]} \quad (3)$$

Here,  $\sigma_0$  is the average photoconductivity due to the average intensity  $I_0$ ,  $E_D = (k_B T/e)K$  is the diffusion field,  $L_D$  is the carrier diffusion length given by  $L_D^2 = (k_B T/e)\mu\tau$ , and  $\mu$  is the carrier mobility. The important quantity for experiments is the amplitude of the photo-emf current given by<sup>3</sup>

$$|J^{\omega}| = \frac{m^2 \Delta}{2} \sigma_0 E_D \frac{\omega\tau_M}{\sqrt{(1 - \omega^2\tau\tau_M)^2 + \omega^2[\tau + \tau_M(1 + K^2 L_D^2)]^2}} \quad (4)$$

One limiting case occurs when the carrier lifetime is much shorter than the dielectric relaxation time and the frequencies of interest are much lower than the inverse carrier lifetime ( $\omega\tau \ll 1$ ). This is true for experiments with GaAs detectors. In that case, Equation (4) can be simplified to obtain<sup>2,3</sup>

$$|J^\omega| = \frac{m^2 \Delta}{2} \sigma_0 E_D \frac{\omega \tau_M}{\sqrt{1 + \omega^2 [\tau_M (1 + K^2 L_D^2)]^2}}. \quad (5)$$

To maximize the photo-emf current amplitude, the fringe spacing is chosen to match the carrier diffusion length such that  $K^2 L_D^2 \cong 1$  in experiments. In addition, the phase modulation frequency should be higher than the inverse dielectric relaxation time ( $\omega \tau_M \gg 1$ ). Under these conditions, the maximum value of the photo-emf current amplitude is

$$|J^\omega|_{\max} = \frac{m^2 \Delta}{4} \sigma_0 E_D \quad (6)$$

The other limiting case is the reverse of the previous one: the carrier lifetime is much longer than the dielectric relaxation time. In addition, the frequencies of interest are much lower than the inverse dielectric relaxation time ( $\omega \tau_M \ll 1$ ). These conditions correspond to experiments with Si detectors. Simplification of Equation (4) under these conditions gives

$$|J^\omega| = \frac{m^2 \Delta}{2} \sigma_0 E_D \frac{\omega \tau_M}{\sqrt{1 + \omega^2 \tau^2}} \quad (7)$$

The phase modulation frequency should exceed the inverse carrier lifetime to maximize the photo-emf current amplitude. For  $\omega \tau \gg 1$ , the photo-emf current amplitude is given by

$$|J^\omega|_{\max} = \frac{m^2 \Delta}{2} \sigma_0 E_D \frac{\tau_M}{\tau} \quad (8)$$

When compared to Equation (6), the photo-emf current amplitude has an extra factor of  $\tau_M / \tau$ , which is much smaller than unity. This is the fundamental reason for the weak photo-emf effect in Si.

### 3. Dember Photocurrent

When the generation of carriers in a semiconductor is nonuniform and there is a carrier density gradient, a diffusion current flows under a short circuit condition. This is related to the Dember effect that is typically observed under open circuit conditions<sup>1, 13, 14</sup>. The current density in the single-carrier case is

$$J = e\mu n(x)E(x) + k_B T \mu \frac{dn(x)}{dx}. \quad (9)$$

where  $n(x)$  is the carrier concentration and  $E(x)$  is the space charge field. Under steady-state conditions, this current density cannot have a spatial variation because that would violate the equation of continuity. Rearranging Equation (9), we can write the space charge field as

$$E(x) = \frac{J - k_B T \mu \frac{dn(x)}{dx}}{e\mu n(x)} \quad (10)$$

The short circuit condition means that there is no voltage drop between the two ends of the semiconductor, so that  $\int_{x_1}^{x_2} E(x) dx = 0$ .

The carrier concentration can be written as the sum of the thermal equilibrium carrier concentration and the excess carrier concentration generated by illumination, as  $n(x) = n_0 + \Delta n(x)$ . The space charge field then becomes

$$E(x) = \frac{J - k_B T \mu \frac{d\Delta n(x)}{dx}}{\sigma_d + e\mu \Delta n(x)} \quad (11)$$



where  $\sigma_d = e\mu n_0$  is the dark conductivity. The short circuit condition yields

$$\int_{x_1}^{x_2} E(x) dx = J \int_{x_1}^{x_2} \frac{dx}{\sigma_d + e\mu\Delta n(x)} - \frac{k_B T}{e} \ln \left[ \frac{\sigma_d + e\mu\Delta n(x_2)}{\sigma_d + e\mu\Delta n(x_1)} \right] = 0. \quad (12)$$

The Dember photocurrent is then given by

$$J = \frac{k_B T}{e} \ln \left[ \frac{\sigma_d + e\mu\Delta n(x_2)}{\sigma_d + e\mu\Delta n(x_1)} \right] \frac{1}{\int_{x_1}^{x_2} \frac{dx}{\sigma_d + e\mu\Delta n(x)}}. \quad (13)$$

If the excitation level is low ( $\Delta n \ll n_0$ ), Equation (13) simplifies to

$$J = k_B T \mu \frac{\Delta n(x_2) - \Delta n(x_1)}{x_2 - x_1}. \quad (14)$$

### 3.1. Uniform Illumination with Increasing Area

Next, we consider the case of spatially uniform illumination whose area is controlled by the shadow of a razor blade. The razor blade is translated from one contact to the other and its edge, taken to be located at  $x = 0$ , can be represented by a bright-dark boundary that moves across the detector surface. This allows the area of illumination to start from zero and increase to cover the whole detector.

The distribution of excess carrier concentration has been solved by Rvykin for this case<sup>1</sup>. In the illuminated region between  $-x_R$  and zero, where  $x_R$  is the distance between the contact on the illuminated side of the detector and the edge of the razor blade, the excess carrier concentration is given by

$$\Delta n_1(x) = \frac{1}{2} g_0 \tau \left[ \left( 1 - e^{x/L_D} \right) + \left( 1 - e^{-\frac{x_R+x}{L_D}} \right) \right]. \quad (15)$$

where  $g_0$  is the average generation rate. In the dark region ( $x > 0$ ), the excess carrier concentration is given by

$$\Delta n_2(x) = \frac{1}{2} g_0 \tau \left( 1 - e^{-x_R/L_D} \right) e^{-x/L_D}. \quad (16)$$

The position of the second contact is  $L - x_R$  and  $x_R$  goes from zero to  $L$  as the razor blade is translated across the detector.

Using the excess carrier concentrations given by Equations (15) and (16), we need to evaluate the integrals

$$\begin{aligned} \int_{x_1}^{x_2} \frac{dx}{\sigma_d + e\mu\Delta n(x)} &= \int_{-x_R}^0 \frac{dx}{\sigma_d + e\mu\Delta n_1(x)} + \int_0^{L-x_R} \frac{dx}{\sigma_d + e\mu\Delta n_2(x)} \\ &= I_1 + I_2 \end{aligned} \quad (17)$$

to be able to calculate the Dember photocurrent. The calculation is summarized in Appendix A.

The result for the first integral is

$$I_1 = \frac{L_D}{\sigma_0} \frac{1}{A} \ln \left| \frac{A - \frac{\sigma_d}{\sigma_0} A - e^{-x_R/L_D} + \frac{\sigma_d + \sigma_0}{\sigma_0}}{A + \frac{\sigma_d}{\sigma_0} A + e^{-x_R/L_D} - \frac{\sigma_d + \sigma_0}{\sigma_0}} \right| \quad (18)$$

where  $\sigma_0 = e\mu g_0 \tau$  is the average conductivity due to the illumination and  $A$  is a constant given by

$$A^2 = \left( \frac{\sigma_d + \sigma_0}{\sigma_0} \right)^2 - e^{-x_R/L_D}. \quad (19)$$

Using Equation (16) in the second integral of Equation (17), we obtain

$$I_2 = \frac{L_D}{\sigma_d} \ln \left[ \frac{\sigma_d e^{(L-x_R)/L_D} + \frac{\sigma_0}{2} (1 - e^{-x_R/L_D})}{\sigma_d + \frac{\sigma_0}{2} (1 - e^{-x_R/L_D})} \right]. \quad (20)$$

Using Equations (15) and (16), the carrier concentration at the illuminated contact at  $x = -x_R$  is

$$\Delta n_1(-x_R) = \frac{1}{2} g_0 \tau (1 - e^{-x_R/L_D}) \quad (21)$$

and the carrier concentration at the dark contact at  $x = L - x_R$  is

$$\Delta n_2(L - x_R) = \frac{1}{2} g_0 \tau (e^{x_R/L_D} - 1) e^{-L/L_D}. \quad (22)$$

Substituting these results into Equation (13), we obtain the final expression for the Dember photocurrent as

$$J = \frac{k_B T}{e} \frac{1}{I_1 + I_2} \ln \left[ \frac{\sigma_d + \frac{\sigma_0}{2} (e^{x_R/L_D} - 1) e^{-L/L_D}}{\sigma_d + \frac{\sigma_0}{2} (1 - e^{-x_R/L_D})} \right] \quad (23)$$

where  $I_1$  and  $I_2$  are the two integrals given by Equations (18) and (20), respectively.

### 3.2. Oscillating Interference Pattern

The rate equation for the carrier concentration is

$$\frac{\partial \Delta n(x, t)}{\partial t} = g(x, t) - \frac{\Delta n(x, t)}{\tau} + \frac{1}{e} \frac{\partial J(x, t)}{\partial x} \quad (24)$$

where  $g(x, t)$  is the photogeneration rate of carriers. It is given by  $g(x, t) = \alpha I(x, t)/h\nu$  where  $\alpha$  is the absorption coefficient,  $I(x, t)$  is the intensity of the interference pattern illuminating the detector, and  $h\nu$  is the photon energy. The space charge field has negligible influence on the carrier distribution because the dielectric relaxation time is very short compared to  $\omega^{-1}$  and the space charge density redistributes itself in a short time<sup>1</sup>. Substituting Equation (9) for the current density and neglecting the term with the space charge field gives a linear partial differential equation for the carrier concentration

$$D \frac{\partial^2 \Delta n(x, t)}{\partial x^2} - \frac{\partial \Delta n(x, t)}{\partial t} - \frac{\Delta n(x, t)}{\tau} = -g(x, t) \quad (25)$$

where  $D = \mu(k_B T/e)$  is the diffusion coefficient.

The detector is illuminated by an interference pattern that is blocked by the contact metal in the region  $x > 0$  and  $x < -L$ . Here, we represent the intensity of the interference pattern by

$$I(x, t) = I_0 [1 + m \cos(Kx + \phi + \Delta \cos \omega t)] \quad (26)$$

where  $\phi$  determines which part of the interference pattern falls on the metal-semiconductor boundary at  $x = 0$  in the absence of phase modulation ( $\Delta = 0$ ). If the amplitude of the phase modulation  $\Delta$  is much smaller than unity, the intensity of the interference pattern can be written as

$$\begin{aligned} I(x, t) &\cong I_0 + mI_0 [\cos(Kx + \phi) - \Delta \sin(Kx + \phi) \cos \omega t] \\ &= I_0 + mI_0 \cos(Kx + \phi) - \left[ \frac{m\Delta}{2} I_0 \sin(Kx + \phi) e^{j\omega t} + \text{c.c.} \right] \end{aligned} \quad (27)$$

where we have used the approximations  $\cos(\Delta) \cong 1$  and  $\sin(\Delta) \cong \Delta$  to obtain the first line. Because Equation (25) is linear, the carrier concentration can be expanded using the same frequency dependence:

$$\Delta n(x, t) = \Delta n_0(x) + \left( \frac{\Delta n_\omega(x)}{2} e^{j\omega t} + \text{c.c.} \right). \quad (28)$$

Substituting Equations (27) and (28) into Equation (25) and collecting terms at zero frequency gives

$$\frac{d^2 \Delta n_0(x)}{dx^2} - \frac{\Delta n_0(x)}{L_D^2} = -\frac{g_0 \tau}{L_D^2} [1 + m \cos(Kx + \phi)] \quad (29)$$

where  $g_0 = \alpha I_0 / h \nu$  and both sides of the equation have been divided by the diffusion coefficient  $D$ . Similarly, collecting terms at frequency  $\omega$  and dividing both sides by  $D$  yields the following ordinary differential equation for  $\Delta n_\omega(x)$ :

$$\frac{d^2 \Delta n_\omega(x)}{dx^2} - \frac{1 + j\omega\tau}{L_D^2} \Delta n_\omega(x) = \frac{g_0 \tau m \Delta}{L_D^2} \sin(Kx + \phi). \quad (30)$$

Appendix B outlines the method of solution for Equations (29) and (30). The final solutions of Equation (29) in the dark and illuminated regions are

$$\begin{aligned} \Delta n_0(x) = & \frac{1}{2} g_0 \tau (1 - e^{-L/L_D}) e^{-x/L_D} + \frac{1}{2} \frac{m g_0 \tau}{1 + K^2 L_D^2} \\ & \times \{ K L_D \sin \phi + \cos \phi - e^{-L/L_D} [\cos(-KL + \phi) + K L_D \sin(-KL + \phi)] \} e^{-x/L_D} \end{aligned} \quad (31)$$

for  $x > 0$ ,

$$\Delta n_0(x) = \frac{1}{2} g_0 \tau (e^{L/L_D} - 1) e^{x/L_D} + \frac{1}{2} \frac{m g_0 \tau}{1 + K^2 L_D^2} \times \{ K L_D \sin \phi - \cos \phi + e^{L/L_D} [\cos(-KL + \phi) - K L_D \sin(-KL + \phi)] \} e^{x/L_D} \quad (32)$$

for  $x < -L$ , and

$$\Delta n_0(x) = -\frac{1}{2} g_0 \tau (e^{x/L_D} + e^{-(x+L)/L_D}) + \frac{1}{2} \frac{m g_0 \tau}{1 + K^2 L_D^2} \times \{ (-\cos \phi + K L_D \sin \phi) e^{x/L_D} - [\cos(-KL + \phi) + K L_D \sin(-KL + \phi)] e^{-(x+L)/L_D} \} \quad (33)$$

$$+ g_0 \tau + \frac{m g_0 \tau}{1 + K^2 L_D^2} \cos(Kx + \phi)$$

for  $-L < x < 0$ .

The final solutions of Equation (30) in the dark and illuminated regions are

$$\Delta n_\omega(x) = \frac{1}{2} \frac{m \Delta g_0 \tau}{1 + K^2 L_D^2 + j\omega\tau} \left\{ \frac{K L_D}{\sqrt{1 + j\omega\tau}} \cos \phi - \sin \phi + \left[ \sin(-KL + \phi) - \frac{K L_D}{\sqrt{1 + j\omega\tau}} \cos(-KL + \phi) \right] e^{-L\sqrt{1 + j\omega\tau}/L_D} \right\} e^{-x\sqrt{1 + j\omega\tau}/L_D} \quad (34)$$

for  $x > 0$ ,

$$\Delta n_\omega(x) = \frac{1}{2} \frac{m \Delta g_0 \tau}{1 + K^2 L_D^2 + j\omega\tau} \left\{ \frac{K L_D}{\sqrt{1 + j\omega\tau}} \cos \phi + \sin \phi - \left[ \sin(-KL + \phi) + \frac{K L_D}{\sqrt{1 + j\omega\tau}} \cos(-KL + \phi) \right] e^{L\sqrt{1 + j\omega\tau}/L_D} \right\} e^{x\sqrt{1 + j\omega\tau}/L_D} \quad (35)$$

for  $x < -L$ , and

$$\Delta n_{\omega}(x) = \frac{m\Delta g_0\tau}{1+K^2L_D^2+j\omega\tau} \left\{ \frac{1}{2} \left( \frac{KL_D}{\sqrt{1+j\omega\tau}} \cos\phi + \sin\phi \right) e^{x\sqrt{1+j\omega\tau}/L_D} \right. \\ \left. + \frac{1}{2} \left[ \sin(-KL+\phi) - \frac{KL_D}{\sqrt{1+j\omega\tau}} \cos(-KL+\phi) \right] e^{-(x+L)\sqrt{1+j\omega\tau}/L_D} - \sin(Kx+\phi) \right\} \quad (36)$$

for  $-L < x < 0$ .

The Dember photocurrent, given by Equation (14), will consist of a DC component and an AC component at frequency  $\omega$ . The current density can be written as

$$J(t) = J_0 + \left( \frac{J_{\omega}}{2} e^{j\omega t} + \text{c.c.} \right) \quad (37)$$

where the DC component of the current is

$$J_0 = k_B T \mu \frac{\Delta n_0(x_2) - \Delta n_0(x_1)}{x_2 - x_1} \quad (38)$$

and the AC component at frequency  $\omega$  is

$$J_{\omega} = k_B T \mu \frac{\Delta n_{\omega}(x_2) - \Delta n_{\omega}(x_1)}{x_2 - x_1}. \quad (39)$$

The carrier concentrations at the contacts are

$$\Delta n_0(0) = \frac{1}{2} g_0 \tau (1 - e^{-L/L_D}) + \frac{1}{2} \frac{m g_0 \tau}{1 + K^2 L_D^2} \{ KL_D \sin\phi + \cos\phi \\ - e^{-L/L_D} [KL_D \sin(-KL+\phi) + \cos(-KL+\phi)] \} \quad (40)$$

$$\Delta n_0(-L) = \frac{1}{2} g_0 \tau (1 - e^{-L/L_D}) + \frac{1}{2} \frac{m g_0 \tau}{1 + K^2 L_D^2} \left\{ e^{-L/L_D} (K L_D \sin \phi - \cos \phi) + [-K L_D \sin(-KL + \phi) + \cos(-KL + \phi)] \right\} \quad (41)$$

$$\Delta n_\omega(0) = \frac{1}{2} \frac{m \Delta g_0 \tau}{1 + K^2 L_D^2 + j\omega\tau} \left\{ \frac{K L_D}{\sqrt{1 + j\omega\tau}} \cos \phi - \sin \phi + e^{-L\sqrt{1 + j\omega\tau}/L_D} \left[ \sin(-KL + \phi) - \frac{K L_D}{\sqrt{1 + j\omega\tau}} \cos(-KL + \phi) \right] \right\} \quad (42)$$

and

$$\Delta n_\omega(-L) = \frac{1}{2} \frac{m \Delta g_0 \tau}{1 + K^2 L_D^2 + j\omega\tau} \left\{ e^{-L\sqrt{1 + j\omega\tau}/L_D} \left[ \frac{K L_D}{\sqrt{1 + j\omega\tau}} \cos \phi + \sin \phi \right] - \left[ \sin(-KL + \phi) + \frac{K L_D}{\sqrt{1 + j\omega\tau}} \cos(-KL + \phi) \right] \right\} \quad (43)$$

Assuming that the detector length is much larger than the diffusion length so that  $\exp(-L/L_D) \cong 0$  in Equations (40) through (43), the DC component of the current density is

$$J_0 = \frac{k_B T}{e} \frac{\sigma_0}{2L} \frac{m}{1 + K^2 L_D^2} \left[ K L_D \frac{1 + \cos KL}{\sin KL} - 1 \right] [\sin KL \sin \phi - (1 - \cos KL) \cos \phi] \quad (44)$$

Similarly, the AC component of the current density is

$$J_\omega = \frac{k_B T}{e} \frac{\sigma_0}{2L} \frac{m \Delta}{1 + K^2 L_D^2 + j\omega\tau} \left[ \frac{K L_D}{\sqrt{1 + j\omega\tau}} \frac{1 + \cos KL}{\sin KL} - 1 \right] \times [\sin KL \cos \phi + (1 - \cos KL) \sin \phi] \quad (45)$$



The optimum grating phase that maximizes the AC component of the Dember photocurrent is given by

$$\tan \phi_{\text{opt}} = \frac{1 - \cos KL}{\sin KL}. \quad (46)$$

Using this value for the grating phase in Equation (45) provides the AC Dember photocurrent density maximized with respect to  $\phi$  as

$$J_{\omega} = \frac{k_B T}{e} \frac{\sigma_0}{2L} \frac{m\Delta}{1 + K^2 L_D^2 + j\omega\tau} \left[ \frac{KL_D}{\sqrt{1 + j\omega\tau}} - \frac{\sin KL}{1 + \cos KL} \right] \sqrt{2(1 + \cos KL)} \quad (47)$$

Figure 2 is a three-dimensional plot of the magnitude of  $J_{\omega}$ , maximized with respect to  $\phi$ , as a function of  $\omega$  and  $K$ . The deeply scalloped nature of the response indicates that the photocurrent response can vary greatly with  $KL$ , or equivalently, the number of interference fringes between the contact electrodes.

#### 4. Experimental Results

We investigated silicon detectors commercially fabricated in the configuration shown in Figure 1(b) on 200 micron thick 7.62 cm (3") high-purity Si wafers from Topsil Semiconductor Materials. High purity wafers were selected because their resistivities are the closest to that of intrinsic Si among commercially available wafers. The wafers were weakly n-type and had a resistivity specification of 3000 – 7000 Ohm cm. Fabrication started with thermally grown silicon dioxide to passivate the surfaces. Phosphorus was diffused into the areas to be metallized so that ohmic contacts could be formed. Aluminum contacts were deposited onto the areas defined by the same mask used for diffusion. The detector size determined by the contacts was 2

mm by 2 mm. Finally, the wafers were proton implanted in an attempt to reduce the carrier lifetime and increase the photo-emf current. The original carrier lifetime specification for the wafers was 1 ms. After fabrication, the wafers were diced and the detectors were attached and wire bonded to TO-style packages. Our DC current-voltage measurements indicated that the fabricated devices had resistances on the order of  $10\text{ K}\Omega$ .

The experimental setup used to characterize the detectors is shown in Figure 3. We used a CW laser diode (SDL 5722) with a wavelength of 852 nm and collimated its output using a lens (Newport F-L20B). A beamsplitter separated the beam into two arms and one of these was modulated using a phase modulator (ConOptics 350-50). The output current of the detector was amplified with an Analog Modules 341-4 transimpedance amplifier with a transimpedance gain of  $10^6\text{ V/A}$  and a bandwidth of 1.5 MHz.

We first operated the setup in Figure 3 as a Mach-Zehnder interferometer, by making the beam intersection angle  $\theta = 0$  before impinging on the detector. The photocurrent was measured as a function of phase modulation frequency for three different optical power levels. The detection circuit used for this set of measurements was a  $1\text{ K}\Omega$  load resistor and an Analog Modules 351-2 voltage amplifier with a voltage gain of 100. The bias voltage applied to the detector and load resistor was 0.21 V. The measurements were corrected for the frequency response of the phase modulator, which was measured using the same Mach-Zehnder configuration with the detector replaced by a New Focus 1801 photoreceiver. The peak-to-peak amplitude of the phase modulation was  $56.8^\circ$ . Figure 4 shows the results of the measurements as well as theoretical curves for the frequency response of a simple photoconductor. The theoretical dependence used is given by<sup>15</sup>

$$|I(\omega)| = \frac{I_0}{\sqrt{1 + \omega^2 \tau^2}} \quad (48)$$

where  $I_0$  is the low frequency value of the photocurrent. The three curves in Figure 4 are scaled to agree with the low frequency values of the photocurrent but use a single value for the carrier lifetime of 12  $\mu$ s. Based on the good agreement with the experimental data, this provided an estimate of the carrier lifetime of the detector.

Next, we performed an experiment using uniform illumination with increasing area as described theoretically in Section 3.1. The signal beam was blocked and the reference beam was expanded to obtain a nearly uniform intensity profile by using a 10 cm focal length lens placed 81.3 cm away from the detector. A thin metal plate was used to prevent light from reaching the contact that was not covered by the razor blade so that Dember currents from the other sides of the contact did not affect the results. The razor blade was translated in steps of 0.125 mm from one contact towards the other so that the illuminated area increased gradually. Figure 5 shows the results of these measurements as a function of the razor blade translation. The theoretical curve is based on Equation (23) with  $L_D = 205 \mu\text{m}$  and  $\sigma_0 \ll \sigma_d$ . The diffusion length was obtained using the estimated carrier lifetime value of 12  $\mu$ s and an electron mobility of 1350  $\text{cm}^2/\text{Vs}$ . Equation (23) assumes the photo-excited charge carriers are generated uniformly within the sample volume. The optical absorption coefficient for silicon at 852 nm is about 1000  $\text{cm}^{-1}$ . For this experiment the photo-excited charge was generated within the top 10 to 20 microns of the 200 micron thick devices. Consequently, Figure 5 indicates that the agreement of the data with Equation (23) is only qualitatively correct but does exhibit the expected profile of the Dember photocurrent.

The detector response to an oscillating interference pattern was investigated next by measuring the peak amplitude of the sinusoidal component of the photocurrent. The sinusoidal photocurrent amplitude was measured as a function of grating wavenumber at a temporal modulation frequency of 1 KHz. The grating phase was adjusted to maximize the current at each wavenumber using the DC bias voltage on the phase modulator. Figure 6 shows the results of the measurements as well as a theoretical curve based on Equation (47) with  $\omega\tau \ll 1$ . The measurement frequency of 1KHz satisfies the condition  $\omega\tau \ll 1$ , considering the estimated carrier lifetime of 12  $\mu$ s. The results show an oscillation that goes almost as  $\sin(KL)$ , a characteristic of the Dember photocurrent. The circles represent measured data points. These do not fall close to the theoretical curve at low  $K$  values, but do exhibit the scalloped curve behavior of a Dember photocurrent. The theory that yielded Equation (47) assumed constant amplitude plane wave incident optical fields whereas the experiment was done with Gaussian laser beams. Because the Dember current arises from gradients of photo-excited charge carrier concentrations, it is reasonable to expect some departure from plane-wave illumination behavior due to spatial derivatives of the Gaussian optical field amplitudes that is the most pronounced at small values of  $K$  where there is one or fewer complete optical fringes between the electrode contacts. Another reason for the discrepancies may be the inadequacy of a single charge carrier model and ambipolar diffusion length to accurately characterize the Dember photocurrent.

Figure 7 shows the Dember photocurrent as a function of phase modulation frequency for five different values of the grating wavenumber. The grating phase was again adjusted to maximize the current. The frequency response is flat up to a frequency determined by the inverse carrier lifetime and value of  $KL_D$ . Theoretical curves based on Equation (47) are not included because even though the frequency dependence for each curve is modeled well by that equation,

the relative amplitudes for different wavenumbers compares poorly with experiment. The main reason for that is the highly sensitive nature of the Dember photocurrent to the grating wavenumber as demonstrated in Figure 2 and the plane wave assumption in Equation (1).

## 5. Conclusion

The experimental data presented are in good qualitative agreement with the fundamental nature of a photocurrent generated by the Dember effect rather than the PEMF effect. The conclusion is that PEMF photocurrents in semiconductor photoconductors with bulk resistivities less than  $10^4$  ohm-cm and electrode configurations that block light at the metal-semiconductor interface are dominated by Dember photocurrents that are orders of magnitude larger than photocurrents due to the PEMF effect. The dependence of the Dember photocurrents on optical interference fringe spacing and position relative to the contact electrodes is complicated. The frequency dependence of Dember photocurrents is similar to that of an ordinary photoconductor except that the frequency roll-off depends also on the value of  $KL_D$  as well as  $\omega\tau$  ( $K = 0$  corresponds to the usual situation of illumination of a photoconductor with parallel interfering optical beams).

The silicon devices with side electrodes as shown in Figure 1a that were reported earlier<sup>10</sup> to show the PEMF effect were retested for the PEMF effect this time using phase modulated 852 nm light. A small PEMF photocurrent, on the order of a few nanoamperes, was again found provided the illuminated region was kept well centered between the sample edges and did not directly fall on the side contact electrodes. An increase of the illuminated area to include the side electrodes resulted in a mixture of PEMF and Dember photocurrents. The original PEMF experiments at 1064 nm were done with two independent lasers offset in center frequency. This produced a DC PEMF photocurrent that was detected by a high gain ( $10^8$  V/A) transimpedance

amplifier with a frequency response of DC to 20 KHz. The minimum frequency offset used was about 30 KHz which is beyond the frequency range of the amplifier. The experiment would have detected the DC but not the AC component of a Dember photocurrent. Because the observed DC photocurrent fit the expected shape of the PEMF response for fringes moving with constant velocity, it was concluded (perhaps incorrectly) that the entire photocurrent was due to the PEMF effect in silicon.

The conclusion of the measurements reported here is that the photocurrents observed are due to the Dember effect and that any PEMF photocurrent present is too small to be detected in silicon devices with surface electrodes that cause shadowing. Because Dember photocurrents are generated by stationary or slow moving optical intensity gradients that may or may not be caused by phase modulation on one of two mutually coherent interfering optical beams, whereas true PEMF photocurrents are generated only by high speed optical phase modulation and are insensitive to slow or stationary optical intensity gradients, these types of silicon photoconductive detectors appear to be not useful as detectors of optical phase modulation. The use of semitransparent surface electrodes would reduce but not eliminate the presence of the Dember photocurrents.

### **Acknowledgments:**

This material is based upon work supported by, or in part by, the U. S. Army Research Office under grant number DAAD19-00-0048.

### **Appendix**

Using Equation (15) in the first integral of Equation (17), we have

$$I_1 = \int_{-x_R}^0 \frac{e^{x/L_D} dx}{-\frac{\sigma_0}{2} e^{2x/L_D} + (\sigma_d + \sigma_0) e^{x/L_D} - \frac{\sigma_0}{2} e^{-x_R/L_D}} \quad (49)$$

We perform a change of variables  $u = \exp(x/L_D)$ , complete the square in the denominator of the integrand and perform another change of variables  $v = u - (\sigma_d + \sigma_0)/\sigma_0$  to obtain

$$I_1 = \int_{\frac{e^{-x_R/L_D} - \frac{\sigma_d + \sigma_0}{\sigma_0}}^{\frac{1 - \frac{\sigma_d + \sigma_0}{\sigma_0}}{\sigma_0}} \frac{2 \frac{L_D}{\sigma_0} dv}{A^2 - v^2} \quad (50)$$

The result of the integration is given by Equation (18) of Section 3.1.

Equations (29) and (30) are solved by using the method of undetermined coefficients.

The solution of the homogeneous equation for Equation (29) is given by

$$\Delta n_0(x) = C_1 e^{r_1 x} + C_2 e^{r_2 x} \quad (51)$$

where  $r_{1,2} = \pm 1 / L_D$ . Since the non-homogeneous part of Equation (29) is a sum of two terms, the particular solution is also a sum of two solutions. The first one corresponds to the spatially uniform term of the non-homogeneous part and is equal to  $g_0 \tau$ . The second one is a solution of the equation

$$\frac{d^2 \Delta N_0(x)}{dx^2} - \frac{\Delta N_0(x)}{L_D^2} = -\frac{g_0 \tau}{L_D^2} m \cos(Kx + \phi) \quad (52)$$

and is of the form

$$\Delta N_0(x) = A \sin Kx + B \cos Kx \quad (53)$$

The coefficients  $A$  and  $B$  are found by substituting Equation (51) into Equation (50) and equating the coefficients of the sine and cosine terms. The results are

$$A = -\frac{mg_0\tau}{1 + K^2 L_D^2} \sin \phi \quad (54)$$

and

$$B = \frac{mg_0\tau}{1 + K^2 L_D^2} \cos \phi. \quad (55)$$

The particular solution of the full non-homogeneous equation is then given by

$$\Delta N_0(x) = g_0\tau + \frac{mg_0\tau}{1 + K^2 L_D^2} \cos(Kx + \phi). \quad (56)$$

The forms of the solution in the dark regions ( $x > 0$  and  $x < -L$ ) are

$$\Delta n_0(x) = C_2 e^{-x/L_D} \quad (57)$$

and

$$\Delta n_0(x) = C_3 e^{x/L_D} \quad (58)$$

whereas the solution in the illuminated region ( $-L < x < 0$ ) has the form

$$\Delta n_0(x) = C_3 e^{x/L_D} + C_4 e^{-x/L_D} + g_0\tau + \frac{mg_0\tau}{1 + K^2 L_D^2} \cos(Kx + \phi). \quad (59)$$

These solutions satisfy the boundary conditions that the excess carrier concentration remain finite as  $x$  goes to  $\pm\infty$ . The constants  $C_2$ ,  $C_3$ ,  $C_4$ , and  $C_5$  are found by requiring the continuity of



the excess carrier concentration and its first derivative at the boundaries between the dark and illuminated regions. The results are

$$C_2 = \frac{1}{2} g_0 \tau (1 - e^{-L/L_D}) + \frac{1}{2} \frac{mg_0 \tau}{1 + K^2 L_D^2} \times \left\{ \cos \phi + KL_D \sin \phi - e^{-L/L_D} [KL_D \sin(-KL + \phi) + \cos(-KL + \phi)] \right\} \quad (60)$$

$$C_3 = -\frac{1}{2} g_0 \tau + \frac{1}{2} \frac{mg_0 \tau}{1 + K^2 L_D^2} (-\cos \phi + KL_D \sin \phi) \quad (61)$$

$$C_4 = -\frac{1}{2} g_0 \tau e^{-L/L_D} - \frac{1}{2} e^{-L/L_D} \frac{mg_0 \tau}{1 + K^2 L_D^2} [\cos(-KL + \phi) + KL_D \sin(-KL + \phi)] \quad (62)$$

$$C_5 = \frac{1}{2} g_0 \tau (e^{L/L_D} - 1) + \frac{1}{2} \frac{mg_0 \tau}{1 + K^2 L_D^2} \times \left\{ -\cos \phi + KL_D \sin \phi + e^{L/L_D} [-KL_D \sin(-KL + \phi) + \cos(-KL + \phi)] \right\} \quad (63)$$

The solution of the homogeneous equation for Equation (30) is given by

$$\Delta n_w(x) = C_1 e^{r_1 x} + C_2 e^{r_2 x} \quad (64)$$

where  $r_1$  and  $r_2$  are the solutions of the characteristic equation

$$r^2 - \frac{1 + j\omega\tau}{L_D^2} = 0. \quad (65)$$

The two values of  $r$  are given by

$$r_{1,2} = \pm \frac{\sqrt{1 + j\omega\tau}}{L_D^2} = \pm \frac{1}{L_D^2 \sqrt{2}} \left[ \left( \sqrt{1 + \omega^2 \tau^2} + 1 \right)^{1/2} + j \left( \sqrt{1 + \omega^2 \tau^2} - 1 \right)^{1/2} \right] \quad (66)$$

The particular solution of Equation (30) is of the form

$$\Delta N_{\omega}(x) = A \sin Kx + B \cos Kx \quad (67)$$

The coefficients  $A$  and  $B$  are found by substituting Equation (65) into Equation (30) and equating the coefficients of the sine and cosine terms. The results give the particular solution of Equation (30):

$$\Delta N_{\omega}(x) = -\frac{m\Delta g_0 \tau}{1 + K^2 L_D^2 + j\omega\tau} \sin(Kx + \phi). \quad (68)$$

The forms of the solution for Equation (30) in the dark regions ( $x > 0$  and  $x < -L$ ) are

$$\Delta n_{\omega}(x) = C_2 e^{-x\sqrt{1+j\omega\tau}/L_D} \quad (69)$$

and

$$\Delta n_{\omega}(x) = C_5 e^{x\sqrt{1+j\omega\tau}/L_D} \quad (70)$$

whereas the solution in the illuminated region ( $-L < x < 0$ ) has the form

$$\Delta n_{\omega}(x) = C_3 e^{x\sqrt{1+j\omega\tau}/L_D} + C_4 e^{-x\sqrt{1+j\omega\tau}/L_D} - \frac{m\Delta g_0 \tau}{1 + K^2 L_D^2 + j\omega\tau} \sin(Kx + \phi). \quad (71)$$

These solutions satisfy the boundary conditions that the excess carrier concentration remain finite as  $x$  goes to  $\pm\infty$ . The constants  $C_2$ ,  $C_3$ ,  $C_4$ , and  $C_5$  are found by requiring the continuity of the excess carrier concentration and its first derivative at the boundaries between the dark and the illuminated regions. The results are

$$C_2 = \frac{1}{2} \frac{m\Delta g_0 \tau}{1 + K^2 L_D^2 + j\omega\tau} \left\{ \frac{KL_D}{\sqrt{1 + j\omega\tau}} \cos \phi - \sin \phi \right. \\ \left. + \left[ \sin(-KL + \phi) - \frac{KL_D}{\sqrt{1 + j\omega\tau}} \cos(-KL + \phi) \right] e^{-L\sqrt{1 + j\omega\tau}/L_D} \right\} \quad (72)$$

$$C_3 = \frac{1}{2} \frac{m\Delta g_0 \tau}{1 + K^2 L_D^2 + j\omega\tau} \left( \frac{KL_D}{\sqrt{1 + j\omega\tau}} \cos \phi + \sin \phi \right) \quad (73)$$

$$C_4 = \frac{1}{2} \frac{m\Delta g_0 \tau}{1 + K^2 L_D^2 + j\omega\tau} \left[ -\frac{KL_D}{\sqrt{1 + j\omega\tau}} \cos(-KL + \phi) + \sin(-KL + \phi) \right] e^{-L\sqrt{1 + j\omega\tau}/L_D} \quad (74)$$

$$C_5 = \frac{1}{2} \frac{m\Delta g_0 \tau}{1 + K^2 L_D^2 + j\omega\tau} \left\{ \frac{KL_D}{\sqrt{1 + j\omega\tau}} \cos \phi + \sin \phi \right. \\ \left. - \left[ \sin(-KL + \phi) + \frac{KL_D}{\sqrt{1 + j\omega\tau}} \cos(-KL + \phi) \right] e^{L\sqrt{1 + j\omega\tau}/L_D} \right\} \quad (75)$$

## References

1. S. M. Ryvkin, *Photoelectric Effects in Semiconductors* (Consultants Bureau, New York, 1964).
2. M. P. Petrov, I. A. Sokolov, S. I. Stepanov, and G. S. Trofimov, "Non-steady-state photoelectromotive-force induced by dynamic gratings in partially compensated photoconductors," *J. Appl. Phys.*, **68**, 2216-2225 (1990).

3. S. Stepanov, "Photo-electromotive-force effect in semiconductors," in *Handbook of Advanced Electronic and Photonic Materials and Devices*, Vol. 2, *Semiconductor Devices*, H. S. Nalwa, ed. (Academic Press, London, U.K., 2001), pp. 205-272.
4. C. C. Wang, F. Davidson, and S. Trivedi, "Simple laser velocimeter that uses photoconductive semiconductors to measure optical frequency differences," *Appl. Opt.*, **34**, 6496-6499 (1995).
5. G. J. Dunning, D. M. Pepper, M. P. Chiao, P. V. Mitchell, and F. M. Davidson, "Optimizing the photo-EMF response for high-speed compensation and broadband laser-based ultrasonic remote sensing," in *Conference on Lasers and Electro-Optics*, OSA Technical Digest Series (Optical Society of America, Washington, D. C., 1997), pp. 45-46.
6. R. J. Dewhurst and Q. Shan, "Optical remote measurement of ultrasound," *Meas. Sci. Technol.*, **10**, R139-R168 (1999).
7. N. A. Korneev and S. I. Stepanov, "Non-steady-state photoelectromotive force in semiconductor crystals with high light absorption," *J. Appl. Phys.*, **74**, 2736-2741 (1993).
8. F. M. Davidson, C. C. Wang, C. T. Field, and S. Trivedi, "Photocurrents in photoconductive semiconductors generated by a moving space-charge field," *Opt. Lett.*, **19**, 478-480 (1994).
9. J. A. Coy, D. D. Nolte, G. J. Dunning, D. M. Pepper, B. Pouet, G. D. Bacher, and M. B. Klein, "Asymmetric interdigitated metal-semiconductor-metal contacts for improved adaptive photoinduced-electromotive-force detectors," *J. Opt. Soc. Am. B*, **17**, 697-704 (2000).
10. C. C. Wang, F. Davidson, and S. Trivedi, "Moving space-charge field effects in photoconductive semiconductors with interband optical excitation of free charge carriers," *J. Opt. Soc. Am. B*, **14**, 21-26 (1997).

11. I. A. Sokolov and S. I. Stepanov, "Non-steady-state photoelectromotive force in crystals with long photocarrier lifetimes," J. Opt. Soc. Am. B, **10**, 1483-1488 (1993).
12. N. Korneev, S. Mansurova, and S. Stepanov, "Non-steady-state photoelectromotive force in bipolar photoconductors with arbitrary level structure," J. Opt. Soc. Am. B, **12**, 615-620 (1995).
13. Q. Liu, C. Chen, and H. Ruda, "Surface photovoltage in undoped semi-insulating GaAs," J. Appl. Phys., **74**, 7492-7496 (1993).
14. L. Kronik and Y. Shapira, "Surface photovoltage phenomena: theory, experiment, and applications," Surf. Sci. Rep., **37**, 1-206 (1999).
15. P. Bhattacharya, *Semiconductor Optoelectronic Devices*, (Prentice Hall, Upper Saddle River, N. J., 1997).
16. D. K. Schroder, "Carrier lifetimes in silicon," IEEE Trans. Electron Devices, **44**, 160-170 (1999).

## Figure Captions

Fig. 1. Two configurations of electrodes on photo-emf detectors: (a) side electrodes; (b) top surface electrodes.

Fig. 2. Theoretical plot of the magnitude of the AC Dember photocurrent, maximized with respect to the grating phase  $\phi$ , as a function of phase modulation frequency  $\omega$  and grating wavenumber  $K$ . The frequency axis is normalized to the carrier lifetime  $\tau$  and the wavenumber axis is normalized to the inverse device length  $L$ . The ratio of diffusion length  $L_D$  to the device length is 0.1.

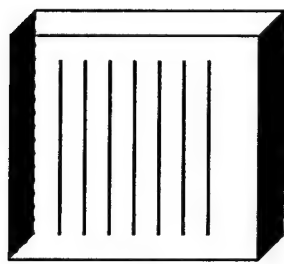
Fig. 3. Experimental setup used to characterize the Dember photocurrent from the detector samples. BS: beamsplitter, M: mirror.

Fig. 4. Frequency dependence of the measured AC photocurrent amplitude in a simple photoconductor configuration. The curves are theoretical plots that use a single value of 12  $\mu$ s for the carrier lifetime. The signal and reference power levels were 5.65 mW and 4.45 mW for the circles, 2.90 mW and 2.30 mW for the squares, and 1.46 mW and 1.14 mW for the triangles, respectively.

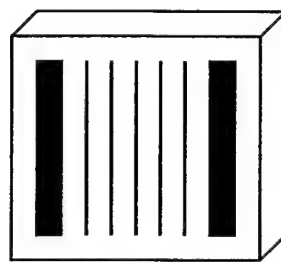
Fig. 5. DC Dember photocurrent under uniform illumination with increasing area. The illuminated area was controlled by the translation of a razor blade that went from covering the whole detector at zero to revealing the area between the two contacts at 2 mm. The circles are experimental data points and the curve is a theoretical plot using  $L_D = 205 \mu$ m.

Fig. 6. Amplitude of the AC Dember photocurrent as a function of grating wavenumber at a phase modulation frequency of 1 KHz. The grating phase was adjusted to maximize the current at each wavenumber. The circles are experimental data points and the curve is a theoretical plot. The signal and reference beam power levels were 2.70 mW and 2.25 mW, respectively.

Fig. 7. Amplitude of the AC Dember photocurrent amplitude as a function of phase modulation frequency for five different values of the grating wavenumber. The grating phase was adjusted to maximize the current at each frequency. The signal and reference beam power levels were 2.65 mW and 2.20 mW, respectively.



(a)



(b)



